PHYSICAL REVIEW B **85**, 214118 (2012)

Thickness dependence of the martensitic transformation, magnetism, and magnetoresistance in epitaxial Ni-Mn-Sn ultrathin films

A. Auge,[*] N. Teichert, M. Meinert, G. Reiss, and A. Hütten
Department of Physics, Thin Films and Physics of Nanostructures, Bielefeld University, 33501 Bielefeld, Germany

E. Yüzüak, I. Dincer, and Y. Elerman
Department of Engineering Physics, Faculty of Engineering, Ankara University, 06100 Besevler, Ankara, Turkey

I. Ennen and P. Schattschneider
Institute of Solid State Physics, Vienna University of Technology, A-1040 Vienna, Austria

(Received 23 September 2011; revised manuscript received 2 April 2012; published 19 June 2012)

We investigate the influence of the film thickness on the martensitic transformation for the example of Ni-Mn-Sn thin films. Epitaxial films with thicknesses ranging from 100 nm down to 10 nm were deposited on MgO by co-sputtering on heated substrates. The martensitic transformation is investigated using temperature dependent x-ray diffraction, magnetization and resistivity measurements. X-ray diffraction and transmission electron microscopy is used to study the growth and the martensitic structure of the films. We find that the martensitic transformation temperatures reduce and the transformation range increases with decreasing film thickness. We show that the transformation is still possible down to a film thickness of 10 nm. A systematic study on the resistance change caused by the martensitic transformation implies that the transformation is suppressed close to the interfaces to the MgO.

DOI: 10.1103/PhysRevB.85.214118 PACS number(s): 81.30.Kf, 72.15.Eb, 75.70.−i, 75.80.+q

I. INTRODUCTION

The functional behavior of shape memory alloys as used for, for example, actuators and switching devices, is related to the structural instability known as martensitic transformation (MT). It is defined as a displacive, diffusionless first-order solid to solid phase transformation from the high temperature austenite to the low temperature martensite phase. Ferromagnetic shape memory alloys (FSMA) are materials that combine the shape memory effect and ferromagnetic behavior. The Heusler alloys Ni_2MnGa and off stoichiometric $Ni_{50}Mn_{25+x}Z_{25-x}$, where Z = In, Sn, are important examples of FSMA due to their interesting physical phenomena such as large magnetic field induced strain,[1] giant magnetocaloric effects,[2] and giant magnetoresistance.[3] For applications such as actuators, magnetic cooling, and hybrid systems, thin films are often mandatory. A general knowledge of how the behavior of the MT changes in thin films compared to the bulk is required for all these applications. Theoretical as well as experimental studies have shown that the transformation behavior as well as the microstructure changes significantly in thin films.[4,5] In investigations on the transformation behavior a broader transition as well as a change in the transition temperature has been found. The broadening of the transition as well as a reduced transition temperature can be caused by substrate constraints,[6] confinement of the nucleus, and size scale effects on the the mean free path of transition dislocations.[5] An increase in the transition temperature can be attributed to stress induced by the lattice mismatch between substrate and thin film.[4]

The details of the microstructure depend strongly on material properties and external influences. In thin films the substrate as well as induced texture play a major role. The degree and kind of texture has a large influence on the allowed variants.[7] A rigid substrate leads to symmetry breaking effects in the sense that not all orientations of the habit planes allow coarsening of nanotwinned martensite to macroscopic nonmodulated variants.[8]

Systematic studies on the influence of the film thickness on the MT are sparse in the literature. Epitaxial Ni-Mn-Ga films have been investigated in the thickness range of 150 to 500 nm with varying stoichiometry.[8] An increasing influence of the substrate with decreasing thickness has been found due to stress induced martensite at the interface. Polycrystalline Ni-Mn-Sn films grown on Si have been investigated in the thickness range from 120 nm up to 2.5 μm by Vishnoi *et al.*[9] They found a suppression of the MT below 410 nm and an increasing transition temperature with increasing film thickness. Most other studies on the MT in thin films investigated a single film thickness in the range of several 100 nm up to several μm.[4,10–13]

In order to investigate the influence of confinement and size scale effects, Ni-Mn-Sn is chosen as a model system. Ni-Mn-Sn is a Heusler alloy with a very low lattice mismatch of 0.7% with respect to MgO[14] and thus a negligible stress influence is expected. The bulk martensite phase of Ni-Mn-Sn has been investigated in former studies. Krenke *et al.*[14] showed that with decreasing valence electron concentration e/a either $L1_0$, 14M, or 10M phase can be observed. 4O, 6M, and 10M structures were measured in works of Sutou *et al.*[15] for $Ni_{50}Mn_{37}Sn_{13}$. The description of the supercells in the former investigations as well as in this study are according to the work of Otsuka *et al.*[16] The unit cell in the martensitic phase is either monoclinic, orthorhombic, or tetragonal.

This paper is organized as follows: In the first section the crystal structure of the martensitic phase is determined for an epitaxial 100 nm thick Ni-Mn-Sn film grown on MgO. The

©2012 American Physical Society

MT is investigated in the following by temperature dependent x-ray diffraction, magnetization, and electric transport measurements in the film thickness range of 100 nm down to 10 nm.

II. EXPERIMENTAL DETAILS

The Ni-Mn-Sn films are grown on MgO(001) substrates using an ultrahigh vacuum (UHV) sputtering system with a base pressure typically better than 1×10^{-9} mbar. The 3 in. sputter sources are arranged in a confocal sputter-up geometry with a target to substrate distance of 21 cm. The inclination of the sources is 30°. The thin film is deposited from elemental Ni, Mn, and Sn targets with a purity of 4N. During deposition the substrate is heated to a temperature of 600 °C and rotated at 10 rpm. The sputtering pressure is set to 2.3×10^{-3} mbar. The deposition rate is 0.32 nm/s. The films are capped by a 2 nm MgO layer deposited by e-beam evaporation. The stoichiometry of the thin films is determined via x-ray fluorescence (XRF) measurements. X-ray diffraction (XRD) in a temperature range from room temperature (RT) up to 400 K is used to determine the crystalline structure. The film thickness is determined by x-ray reflectometry (XRR). The microstructure of the thin films is examined by transmission electron microscopy (TEM). The magnetization of the thin films is investigated using a superconducting quantum interference device magnetometer (Quantum Design MPMS) in the temperature range between 10 and 330 K. The temperature dependence of the field cooled (FC) and field heated (FH) magnetization curves are measured in magnetic fields of 15 mT. The magnetic field is applied parallel to the thin film surface during magnetization measurements. For resistivity and magnetoresistance measurements a standard four point setup is used with a temperature range from 20 up to 370 K in a magnetic field of up to 1 T.

III. RESULTS AND DISCUSSION

A. Structural characterization

The stoichiometry of the films is $\mathrm{Ni}_{51.6}\mathrm{Mn}_{34.9}\mathrm{Sn}_{13.5}$, as determined by XRF. For this stoichiometry a martensitic phase is expected at RT,[17] which is confirmed by XRD measurements for a 100 nm thick film. Ni-Mn-Sn is grown epitaxially in the austenite phase and the in-plane relation is MgO [100] ∥ Ni-Mn-Sn [110] as determined by pole figure scans (not shown). The XRD patterns measured at different tilt angles relative to the substrate normal are shown in Fig. 1(a). The substrate is oriented such that the [100] direction of the Ni-Mn-Sn film in the austenite phase is parallel to the beam. At 0° and 2.6° the $(400)_\mathrm{M}$, $(040)_\mathrm{M}$, and $(004)_\mathrm{M}$ peaks of the orthorhombic martensite phase are visible. The lattice constants are $a = 6.156$ Å, $b = 6.005$ Å, and $c = 5.644$ Å. Lattice constants of all phases are described with reference to the cubic $\mathrm{L2}_1$ unit cell. The $(040)_\mathrm{M}$ peak shows a shoulder on the right-hand side, which is due to a broad distribution of the crystallite orientation belonging to the $(004)_\mathrm{M}$ peak. At higher tilt angles additional peaks appear. As we will show below, the additional peaks are probably due to the formation of 4O and 10M superstructures.

The expected reciprocal space map for a commensurate 4O superstructure is presented in Fig. 1(b). Generally such a diffraction pattern consists of two distinct sets of reflections. The first group are intense peaks of the conventional unit cell with reciprocal vectors $\mathbf{a}^*$,$\mathbf{b}^*$, and $\mathbf{c}^*$. The second group are satellite reflections which need an additional vector for indexing. This additional vector is called modulation vector $\mathbf{q}$ and is usually given as

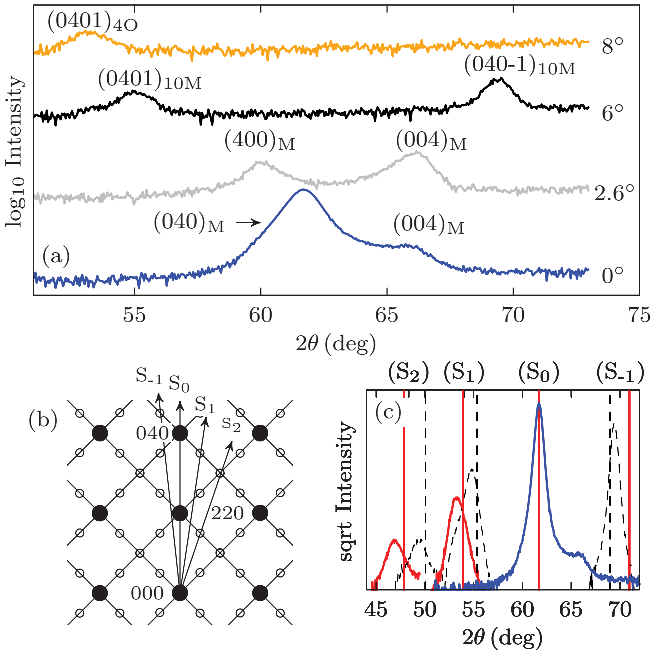

FIG. 1. (Color online) (a) The XRD patterns of the 100 nm thick $\mathrm{Ni}_{51.6}\mathrm{Mn}_{34.9}\mathrm{Sn}_{13.5}$ films at different tilt angles. The reciprocal space map for a commensurate 4O phase is shown in (b). The arrows marked by S_{-1} to S_2 show schematically the 2Θ scans. In (c) the superlattice peaks of the 4O/10M phase and the expected commensurate positions are presented by red solid lines/black dashed lines, respectively.

$$\mathbf{q} = \alpha\mathbf{a}^* + \beta\mathbf{b}^* + \gamma\mathbf{c}^*, \qquad (1)$$

where α, β, and $\gamma \in [0,1]$. For the 4O superstructure three additional diffraction peaks appear in the $\langle 110 \rangle$ directions. The arrows marked by S_{-1} to S_2 show 2θ scans at different tilts. The expected positions for these kind of 2θ scans of commensurate 4O and 10M superstructure peaks are marked by red solid lines and black dashed lines, respectively, in Fig. 1(c). All peaks in the vicinity of the $(040)_\mathrm{M}$ peak, that are measurable in the Bragg-Brentano geometry, are shown. The peak positions do not fit exactly to the expected position of a commensurate superstructure. Thus the superstructure is incommensurate (IC). The tilt angles used to measure the peaks are 18°(18.4°), 14°(14.05°), 8°(8.14°), 6.2°(6.35°), and 5.8°(5.2°). The values in parentheses are the calculated tilt angles for the expected commensurate diffraction spot positions. Similar as in NiMnGa,[18] the modulations are along $\mathbf{c}^*$, which corresponds to the $\langle 110 \rangle_\mathrm{A}$ directions in the austenite crystal structure. For the measured 4O (IC) superstructure the modulation vector is $\mathbf{q}_{4\mathrm{O}} = 0.55\mathbf{c}^*$ and for the 10M (IC) superstructure $\mathbf{q}_{10\mathrm{M}} = 0.42\mathbf{c}^*$. The superstructure peaks at lower 2θ values fit well to $2\mathbf{q}$. The corresponding commensurate modulation lengths would be $\mathbf{q}_{4\mathrm{O}} = \frac{2}{4}\mathbf{c}^* = 0.5\mathbf{c}^*$ and $\mathbf{q}_{10\mathrm{M}} = \frac{2}{5}\mathbf{c}^* = 0.4\mathbf{c}^*$.[18] The incommensurateness δ is usually given by $\mathbf{q}_{4\mathrm{O}} = \gamma_\mathrm{c}(1+\delta)\mathbf{c}^*$, where γ_c is the parameter of a commensurate superstructure. The incommensurateness is $\delta_{4O} = 0.091$ for 4O and $\delta_{10M} = 0.047$ for the 10M superstructures. The 10M superstructure is close to the commensurate value, while the 4O structure shows a larger deviation.

In earlier studies on bulk Ni-Mn-Sn, 4O, 6M, 10M, and 14M superstructures have been found. According to Planes *et al.*[17] the transition from the $L1_0$ to the 14M phase is approximately at $e/a = 8.3$ and from 14M to 10M at $e/a = 8.14$. 4O, 6M, and 10M structures were measured in works of Sutou *et al.*[15] for $Ni_{50}Mn_{37}Sn_{13}$ which has $e/a = 8.11$. The thin films in this study have an e/a value of 8.14, thus the observed superstructures fit well to the literature. The lattice parameters of the orthorhombic phase in this study are similar to the work of Brown *et al.*[19] who investigated $Ni_{50}Mn_{36}Sn_{14}$ ($e/a = 8.08$) and Krenke *et al.*[14] who studied $Ni_{50}Mn_{37}Sn_{13}$ ($e/a = 8.11$). Brown *et al.* determined an orthorhombic structure ($Pmma$) with $a = 6.16$ Å,$b = 6.07$ Å,$c = 5.6$ Å and Krenke *et al.* determined $a = 6.16$ Å,$b = 6.1$ Å,$c = 5.61$ Å for a 10M phase. Larger deviations have been found compared to Sutou *et al.* who found $a = 6.08$ Å,$b = 5.95$ Å,$c = 5.77$ Å for the 4O phase.

The real-space orientation of the observed martensitic unit cells is investigated by pole figure scans of the peaks $(0401)_{10M}$, $(040\text{-}1)_{10M}$, $(0401)_{4O}$, $(400)_M$, $(040)_M$, and $(004)_M$ (shown in Fig. 2). The substrate is oriented such that the [100] MgO direction is at $\varphi = 0°$. Thus $\varphi = 45°$ is the [100] direction of Ni-Mn-Sn in the austenite phase ($[100]_A$). The $(040)_M$ pole figure is dominated by one reflection close to the substrate normal. The pole figures of the $(400)_M$ and $(004)_M$ peaks show four intense reflections in $\langle 100\rangle_A$ orientation indicating four coherent variants. The maximum intensity is at a tilt angle of $\Psi = 2.6°$. Due to an overlap of the $(040)_M$ and the $(400)_M$ peak a strong signal is also seen close to the origin of the $(400)_M$ peak. For the $(004)_M$ the overlap is negligible and variants with considerably less intensity are visible in the $\langle 110\rangle_A$ directions with maximal intensity at a tilt angle of $\Psi = 1.8°$. The pole figures of the 10M superstructure show maximal intensity in the $\langle 100\rangle_A$ orientation at tilt angles of 6.2° and 5.8°, respectively. A much broader signal is measured for the pole figure of $(0401)_{4O}$. It is also oriented in $\langle 100\rangle_A$, but in a broader φ range of about 30°.

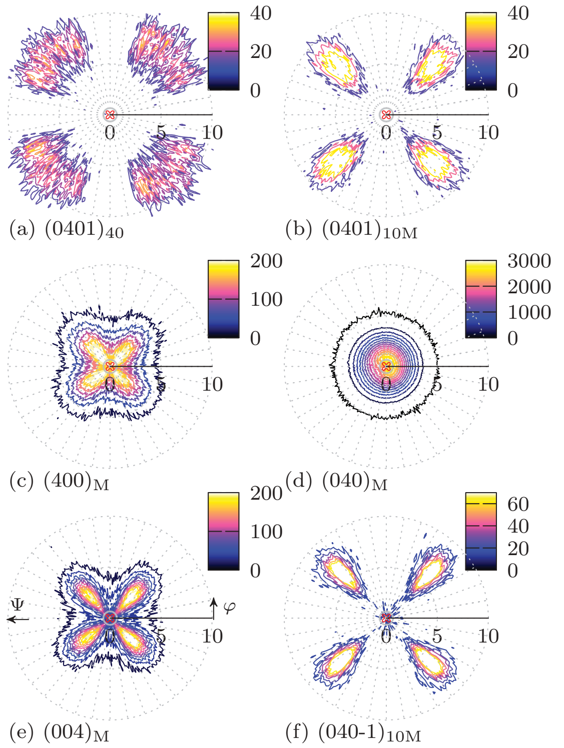

(a) $(0401)_{4O}$ (b) $(0401)_{10M}$

(c) $(400)_M$ (d) $(040)_M$

(e) $(004)_M$ (f) $(040\text{-}1)_{10M}$

FIG. 2. (Color online) Pole figure measurements of the orthorhombic peaks and selected superstructure peaks. The fourfold symmetry verifies epitaxial growth on the MgO substrate.

From investigations of epitaxial Ni-Mn-Ga grown on MgO it is known that a thin austenite film remains at the substrate.[8] This thin austenite layer serves as a habit plane for the martensite. According to the crystallographic theory six variants are possible. However, two of these describe planes perpendicular to the substrate plane requiring an additional coherent interface. This is energetically unfavorable and explains the $\langle 100\rangle_A$ orientation of the main reflections of the orthorhombic phase. The fourfold symmetry also verifies the epitaxial growth on the MgO substrate. The observed tilt angle can be explained by a-c twinning in the (101) plane. For a coherent interface a rotation of the variants is necessary. This rotation or tilt angle Ψ can be calculated by the following relation:[20]

$$\Psi = 45° - \arctan(a_M/c_M). \tag{2}$$

Using the measured lattice parameters Ψ is 2.5°, which is quite close to the measured 2.6°.

The superstructure pole figures show only diffraction spots in $\langle 100\rangle_A$ orientations. This can be explained by the fact that the superstructure spots occur only in $\langle 110\rangle_A$ directions. The broader distribution of $(0401)_{4O}$ in the φ direction could be caused by the higher degree of incommensurateness compared to the 10M modulation leading to additional stacking faults.

The temperature dependence of the structural transformation is measured with XRD for the 100 nm thick film as shown in Fig. 3(a). At 375 K the sample is in the austenite state as seen by the high intensity of the $(004)_A$ peak and the very low intensity of the martensitic peaks. With decreasing temperature the intensity of the $(004)_A$ peak decreases, while the superstructure and orthorhombic peaks become more intense. The martensite start temperature M_s is around 340 K as will also be shown by resistivity measurements. In Fig. 3(b) the normalized integrated intensity of each diffraction spot is shown. The intensities of the superstructure peaks start increasing quite close to M_s. The peaks belonging to the orthorhombic phase start to intensify at around 335 K. The intensity of the 4O peak starts to increase at the same temperature as the 10M phase, but the trend with decreasing temperature is similar to the orthorhombic phase. Above M_s there is a very low intensity for the superstructure peaks, which can be explained by nucleation processes maybe close to defects in the premartensitic phase.

The temperature dependence of the lattice constants is presented in Fig. 3(c). Down to 335 K the thermal contraction of the austenite phase is visible. A linear fit is used to determine the austenite lattice constant $a_{cub} = 5.97$ Å at room temperature. At 345 K the $(400)_M$ and $(004)_M$ peaks of the orthorhombic phase become visible allowing us to determine

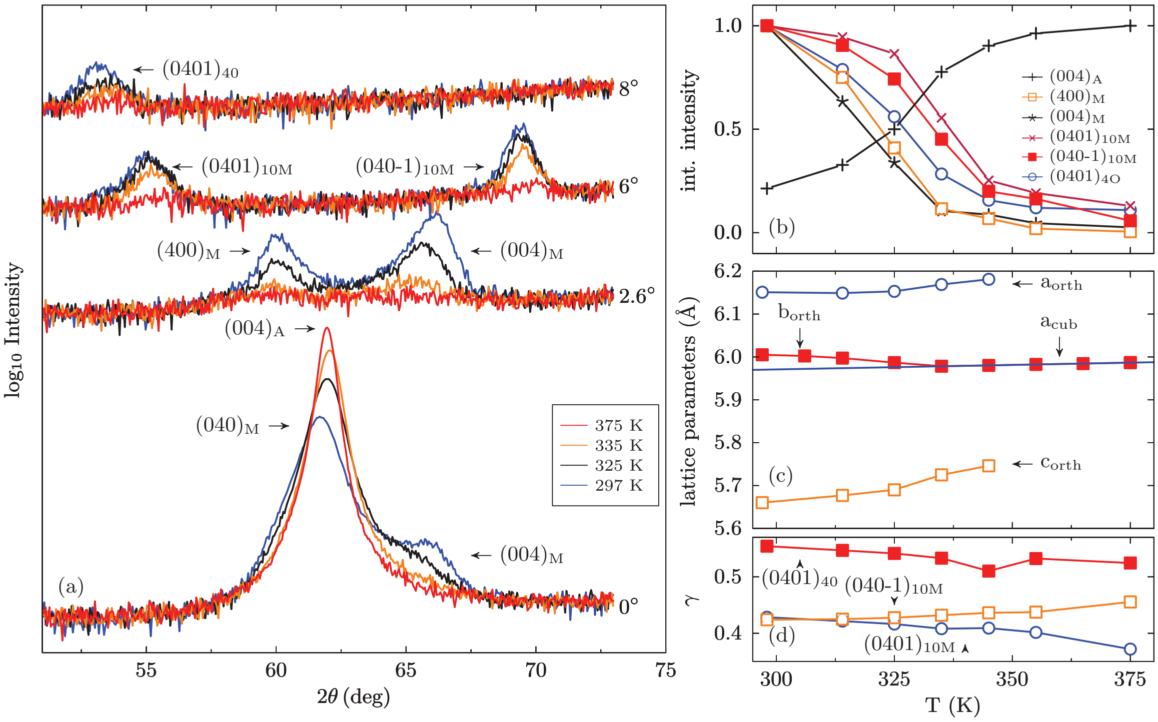

FIG. 3. (Color online) The XRD signal of the structural transformation of the a $Ni_{51.6}Mn_{34.9}Sn_{13.5}$ 100 nm thin film is shown in (a). The normalized integrated intensity of all peaks is plotted in (b). In (c) the temperature dependence of the lattice constants is shown. The temperature dependence of the γ parameter is presented in (d). The sample is measured on the cooling branch of the thermal hysteresis.

a_{orth} and c_{orth}. Both show a decreasing lattice constant down to room temperature. Due to an overlap of the $(004)_A$ and the $(040)_M$ peaks, the lattice constant b_{orth} becomes visible at lower temperatures compared to the other two lattice constants.

The integral width of the $(040)_M$ peak increases by more than a factor of 2 compared to the $(004)_A$ peak. This can be explained by twinning leading to variants smaller than the austenite grain size. Furthermore, a higher degree of microstress can be expected which causes peak broadening as well.

The temperature dependence of the γ parameter of the modulation vectors $\mathbf{q} = \gamma \mathbf{c}^*$ belonging to the superstructure peaks is presented in Fig. 3(d). For the calculation the RT value of $\mathbf{c}^*$ is used since here the only (220) peak is measurable in this setup. With decreasing temperature the following trends are visible: the γ_{4O} parameter of the 4O phase increases. A small dip is visible at 345 K which could be caused by uncertainty of the $\mathbf{c}^*$ value or the development of the orthorhombic phase.

At high temperature the γ_{10M} parameter of the 10M peaks shows an asymmetric modulation length around the $(040)_M$ peak. This asymmetry becomes smaller with decreasing temperature and vanishes around 315 K. Between 335 and 355 K the $(0401)_{10M}$ is close to the commensurate value.

A possible explanation for the asymmetry is based on the modulated lattice relaxation model[21] predicting a shift of the satellite peaks. The model is characterized by two assumptions:

(1) Existence of sharp dip in the transverse phonon dispersion around $\mathbf{q} = 1/3[110]$.

(2) Existence of premartensitic nuclei.

Both assumptions are valid for the investigated sample. A dip in the the TA_2 phonon branch at $\mathbf{q} = 0.35[110]$ has been calculated by Ağduk *et al.*[22] The asymmetry of the modulation vectors is visible in a temperature region before the martensitic transformation starts. This is a premartensitic phase where nuclei like the observed 10M and 4O phase exist. The general trend of an increase of the γ parameter with decreasing temperature has also been observed for a 10M superstructure in Ni-Mn-Ga by Righi *et al.*[18]

A further structural characterization at room temperature is carried out using TEM. In Fig. 4 a TEM image along the $[011]_A$ zone axis of the 100 nm thick film is shown. In some regions nanotwins are visible. Most domains as well as the modulation

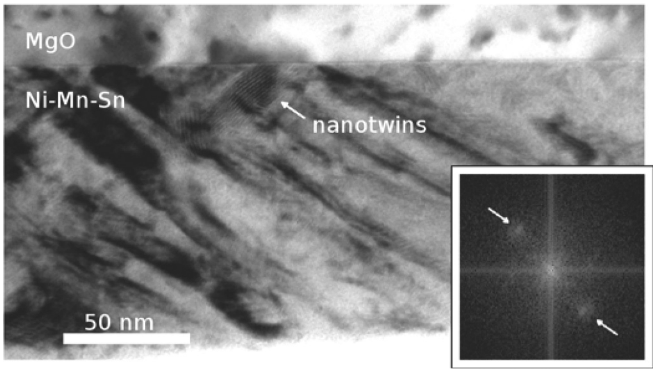

FIG. 4. A TEM image along the $[011]_A$ zone axis of the 100 nm thick Ni-Mn-Sn film at room temperature is shown. A FFT of the region where the nanotwins are visible is shown in the inset. The arrows indicate the features due to the periodicity of the nanotwins.

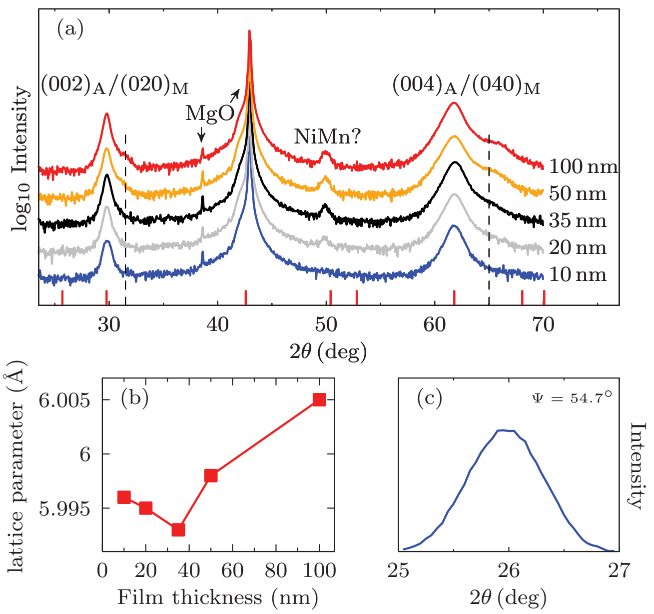

FIG. 5. (Color online) The XRD patterns of the $Ni_{51.6}Mn_{34.9}Sn_{13.5}$ ultrathin films with different thicknesses at room temperature is shown in (a). The red bars show the Bragg positions of the cubic phase. The dashed lines indicate the shoulder positions. The evolution of the lattice parameter with the film thickness is shown in (b). In (c) the (110) reflection of Ni-Mn-Sn is shown.

of the nanotwins show an inclination in the range of 30° to 36° with respect to the MgO surface. This corresponds to (101) twinning planes which viewed from the [011] direction show an inclination of 30°. An FFT shown in the inset of Fig. 4 of the region containing the nanotwins confirms these with a periodicity of approximately 1 nm.

The influence of the film thickness on the structural properties at room temperature is shown in Fig. 5(a). With decreasing film thickness the following trends are visible: the shoulder due to the $(004)_M$ peak on the right side of the $(020)_M$ and $(040)_M$ peak decreases, while the the lattice constant first decreases down to 35 nm film thickness and then increases again up to a maximum of 6.005 Å as shown in Fig. 5(b). Both trends, the decreasing lattice constant and the vanishing shoulder, are comparable to the temperature dependent XRD measurements of the martensitic phase transformation. Thus these results indicate that the structural transformation shifts to lower temperatures with decreasing film thickness as will also be shown by resistivity and magnetization measurements. The expansion of the lattice constant from 35 to 10 nm can be ascribed to a compression of the lattice due to the MgO substrate. The influence of the MgO substrate is reduced with increasing film thickness.

The (110) peak shown in Fig. 5(c) corresponds to the (111) superstructure peak of the $L2_1$ Heusler phase and thus indicates a well ordered $L2_1$ structure. The peak at 49.8° visible in Fig. 5(a) is virtually temperature independent, thus it cannot be a peak of the martensitic phase. It also does not belong to the cubic phase, because the corresponding (311) peak would be at 50.25°. A possible explanation is the presence of a tetragonal NiMn phase[23] due to grain boundary segregation.

To conclude, the temperature dependent XRD measurements show a structural transformation from a cubic austenite phase to a martensitic phase. This transformation is also visible in the thickness dependent XRD measurements indicating a shift to lower martensite start temperatures due to a reduced film thickness. In the following sections the influence of the film thickness on the martensitic transformation will be further investigated by magnetization and resistivity measurements.

B. Magnetic and electric transport characterization

In order to determine the magnetic properties of the $Ni_{51.6}Mn_{34.9}Sn_{13.5}$ thin films and verify the influence of their thickness, temperature dependent FC and FH measurements were performed and the results are shown in Fig. 6. All thin films are ferromagnetic below the austenite Curie temperatures T_C^A which are estimated by differentiation of the magnetization curves. Above 50 K the FH curves do not retrace the FC curves but show a narrow hysteresis for all thin films. This hysteresis is attributed to the martensitic transformation.[14] The transformation temperature range is much wider than for similar bulk alloys.[14] The magnetization of the 10 and 20 nm thin films decreases below around 200 K due to the martensitic transformation. Since the martensitic trans-

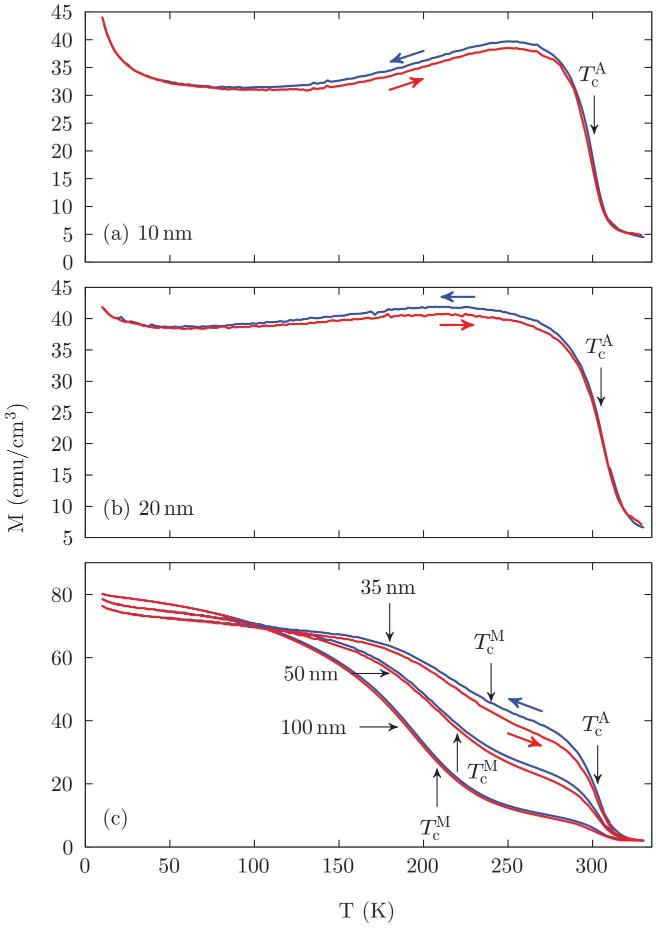

FIG. 6. (Color online) The temperature dependence of FC and FH magnetization curves for $Ni_{51.6}Mn_{34.9}Sn_{13.5}$ thin films with different thicknesses [(a) 10, (b) 20, (c) 35, 50, 100 nm]. The arrows show the temperature change direction.

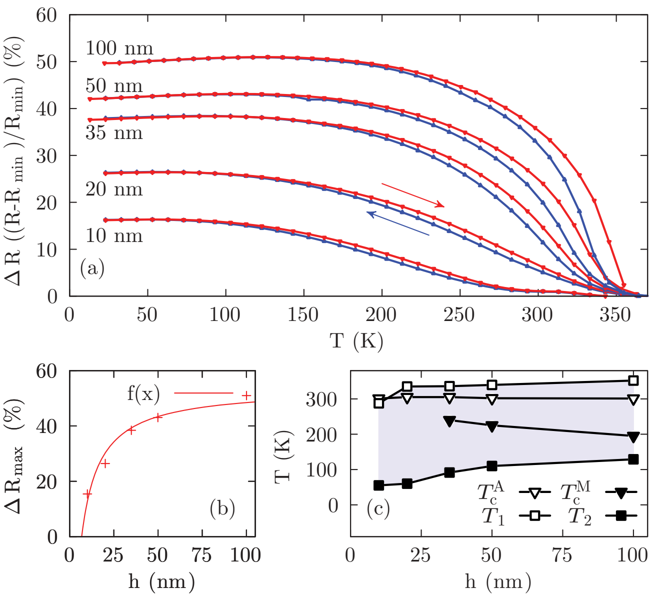

FIG. 7. (Color online) (a) The resistance change over the measured temperature range is plotted for $Ni_{51.6}Mn_{34.9}Sn_{13.5}$ thin films with different thicknesses. The arrows indicate the temperature change direction. In (b) the measured maximal resistance change values for the films and the fit with Eq. (3) is shown. The structural and magnetic phase diagram is presented in (c), where T_1 is defined as $(M_s + A_f)/2$ and T_2 as $(M_f + A_s)/2$.

formation temperatures shift above T_C^A for the 35, 50, and 100 nm thin films [see Fig. 7(c)], the Curie temperatures of the martensite phase T_C^M become visible. While T_C^A is virtually independent of the film thickness, T_C^M increases for decreasing film thickness. This might be due either to different martensitic structures and thus different magnetic couplings between the atoms or an increasing coupling between ferromagnetic austenite and the paramagnetic martensite. The magnetization decreases with decreasing film thickness; the origin of this effect will be investigated in future studies. The upturn of the magnetization curves at low temperatures stems from a paramagnetic contamination of the substrates.

The characteristics of the martensitic transformation are further characterized using temperature dependent resistivity measurements, due to the fact that the Curie temperature is lower than the transformation temperature. The relative changes of the resistance as a function of the temperature, defined as $\Delta R(T) = [R(T) - R_{\min}]/R_{\min}$, for five different film thicknesses are shown in Fig. 7(a). The signs of martensitic transformation, increasing resistance with decreasing temperature and a thermal hysteresis, are clearly visible. Up to a film thickness of 20 nm, one observes a broad range where the slope of $\Delta R(T)$ caused by the transformation is approximately constant. With increasing film thickness the slope of $\Delta R(T)$ becomes steeper and the transformation temperature range is narrowed. The amplitude of the complete resistance change $\Delta R_{\max}$ caused by the transformation reduces by about a factor of 3 from 100 to 10 nm film thickness. The resistance increase due to the martensitic transformation can be linked to superzone boundary effects[24] and defects. A superzone boundary can be caused by structural and magnetic superstructures.[25] In both cases the superstructure leads to a change of the density of electronic states close to the Fermi surface and hence to a change of the resistance. In the case of 35 nm up to 100 nm thick films most of the transformation is in a temperature range above T_C^M. Thus the main impact on the resistance due to superzone boundary effects is caused by structural superstructures. The temperature independent resistivity is quite high as can be seen by the flat progression of the resistivity at low temperatures. This indicates a major contribution of defects due to the formation of twinning planes and dislocations during the transformation. The trend of increasing $\Delta R_{\max}$ with increasing film thickness can be attributed to several factors. One reason is an austenite layer at the MgO interfaces which cannot transform due to the substrate constraint and also differences in the Mn concentration.[20,26] This austenite layer gets a pronounced influence with decreasing film thickness. With this assumption the relative resistance change would be

$$\frac{\Delta R_{\max}}{100} = \frac{h}{h_A + \frac{\rho_A}{\rho_M}(h - h_A)} - 1, \qquad (3)$$

where h is the film thickness and h_A is the thickness of the austenite layer. For the correct description of the h_A using this model the austenite resistivity at low temperatures is required. This is however not accessible with the measured data. The temperature dependence of the resistivity above T_c is very shallow,[27] allowing us to assume a common value ρ_A at 300 K which is used for the fit. The resulting value for h_A is an upper limit. Both $\Delta R_{\max}$ and the fit with Eq. (3) is shown in Fig. 7(b). The fit results in a ratio of $\rho_{M,\approx 100\,K}/\rho_{A,300\,K} = 1.56$ and $h_A < 6.7$ nm. The ratio of $\rho_{M,\approx 100\,K}/\rho_{A,300\,K}$ is comparable to other bulk samples with similar stoichiometry. Koyama *et al.* found 1.48 for $Ni_{50}Mn_{36}Sn_{14}$ $(e/a = 8.08)$.[28] Other possible influences that are not taken into account are different kinds of martensitic structures and effects due to anisotropic conductance in a mixture of austenite and martensite leading to an increasing resistance with decreasing film thickness.[29]

The temperature and magnetic field dependence of the magnetoresistance (MR) is shown in Fig. 8. The negative magnetoresistance is caused by suppression of spin flip scattering close to T_C^A and magnetic field induced reverse transition in the vicinity of the martensitic transformation. The state of the martensitic transformation leads to significant influences on the magnetoresistance. The difference between the cooled down and heated up magnetoresistance resembles the behavior of the magnetization and mirrors the temperature range of the structural transformation.

C. Analysis of the martensitic transformation

The analysis of the MT is done in the following way: The martensite start M_s and austenite finish A_f temperatures are determined by the intersection of the tangents in the beginning of the transformation and the horizontal line at 0%. The martensite finish M_f and austenite start A_s temperatures are determined by the intersection of the tangents at the end of the transformation. The deduced values are shown together with the Curie temperatures in the phase diagram in Fig. 7(c). With decreasing film thickness the following trends are visible: M_s,

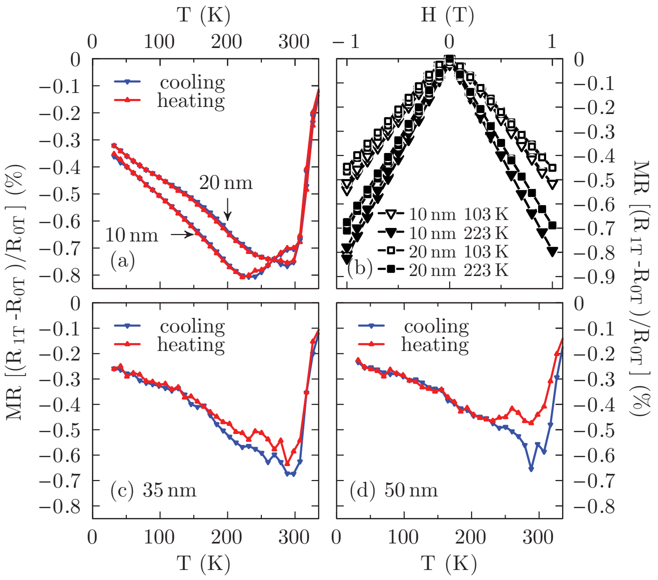

FIG. 8. (Color online) The temperature dependence of the magnetoresistance for a magnetic field of 1 T is plotted for $Ni_{51.6}Mn_{34.9}Sn_{13.5}$ thin films with different thicknesses [(a) 10, 20, (c) 35, and (d) 50 nm]. The magnetic field dependence of magnetoresistance curves for 10 and 20 nm $Ni_{51.6}Mn_{34.9}Sn_{13.5}$ thin films is shown in (b).

A_f, A_s, and M_f temperatures reduce. M_s and A_f decrease by about 18%, whereas M_f and A_s change by about 50%. To compare the M_s temperature for the most bulk-like sample, the 100 nm film, the electron concentration per atom (e/a) value is calculated according to the XRF results. With the e/a value of 8.143 the M_s value is calculated according to the phase diagram for bulk Ni-Mn-Sn samples presented by Krenke *et al.*[30] The resulting M_s temperature is 357 K and thus quite close to the measured value of 347 K.

In literature both trends of increasing and decreasing M_s temperatures have been observed.[4] An increase can be ascribed to stress induced martensite due to a lattice misfit of substrate and the thin film. Since the lattice misfit of MgO and Ni-Mn-Sn is only 0.7% stress induced phenomena are negligible. Instead size scale effects become important. According to Malygin[5] the change of the transformation behavior can be attributed to two different effects: On the one hand, the kinetics of the transformation is influenced by the mean free path of transition dislocations λ. On the other hand, the thermodynamics of the transition is affected by confinement of the martensitic nucleus assumed as disk shaped with diameter l. Both film thickness and grain size become important when the size scale of these are similar to λ and/or to l leading to a hindered martensitic transformation. Meng *et al.* determined the influence of the grain size on the nucleation barrier and critical nucleation size. Below 100 nm grain size a rise of the nucleation barrier and a larger critical nucleus was found.[31] Thus both approaches predict lower M_s temperatures for increasing confinement.

The transition range ΔT_M increases for decreasing film thicknesses up to a maximum of 262 K for 20 nm thick films. For thinner films ΔT_M decreases again. This kind of behavior is predicted by the model of Malygin, if l is larger than λ. However, the Malygin model does not explain the different transformation rates visible both in the resistance and magnetic measurements for the 35 nm up to 100 nm thick films. One reason is that the effect of the substrate is not taken into account which leads to an increase of stored elastic energy during the transformation.[6] Stored elastic energy leads to increased ΔT_M and reduced hysteresis width.[32] This might be the dominant influence for the transformation of the 10 and 20 nm film. The transformation behavior of the thicker films might be explained by a transformation starting in the center of the film and progressing further outside and thus becoming similar to the thinner films. A further influence is a possible variation in the composition leading to different M_s temperatures.

IV. CONCLUSION

To conclude, we have studied the effect of film thickness on the structural, magnetic, and resistance properties of ultrathin Ni-Mn-Sn films deposited on MgO. The ultrathin Ni-Mn-Sn films did show a martensitic phase transformation down to 10 nm film thickness but with a broader transformation range than the bulk. The transformation is suppressed close to the interfaces to the MgO, which becomes visible in the resistance change caused by the MT.

Due to the martensitic transformation in the wide temperature range, these ultrathin films should be a good candidate for future applications of functional nanosystems such as in hybrid magnetocaloric systems.

ACKNOWLEDGMENTS

The authors would like to thank TUBITAK (Project No. 109T582) and International Office of BMBF (Project No. TUR09/I01) for the support. The authors would also like to thank F. Wittbracht, J. Münchenberger for bonding, and P. Thomas for support with XRD measurements. We gratefully acknowledge the possibility to use the Quantum Design MPMS at the Helmholtz-Zentrum Dresden Rossendorf Research Center, Ion Beam Physics and Materials Research Institute, and O. Yildirim and O. Tozkoparan for conducting the measurements.

---

[*] aauge@physik.uni-bielefeld.de

[1] A. Sozinov, A. A. Likhachev, N. Lanska, and K. Ullakko, Appl. Phys. Lett. **80**, 1746 (2002).
[2] P. J. Shamberger and F. S. Ohuchi, Phys. Rev. B **79**, 144407 (2009).
[3] S. Y. Yu, Z. H. Liu, G. D. Liu, J. L. Chen, Z. X. Cao, G. H. Wu, B. Zhang, and X. X. Zhang, Appl. Phys. Lett. **89**, 162503 (2006).
[4] D. C. Dunand and P. Müllner, Adv. Mater. **23**, 216 (2011).
[5] G. A. Malygin, Tech. Phys. **54**, 1782 (2009).
[6] A. L. Roytburd, T. S. Kim, Q. Su, J. Slutsker, and M. Wuttig, Acta Mater. **46**, 5095 (1998).
[7] K. Bhattacharya, *Microstructure of Martensite* (Oxford University Press, Oxford, 2003).

[8] S. Kaufmann, R. Niemann, T. Thersleff, U. K. Rößler, O. Heczko, J. Buschbeck, B. Holzapfel, L. Schultz, and S. Fähler, New J. Phys. **13**, 053029 (2011).

[9] R. Vishnoi, R. Singhal, and D. Kaur, J. Nanopart. Res. **13**, 3975 (2011).

[10] V. Recarte, J. I. Pérez-Landazábal, V. Sánchez-Alárcos, V. A. Chernenko, and M. Ohtsuka, Appl. Phys. Lett. **95**, 141908 (2009).

[11] R. Niemann, O. Heczko, L. Schultz, and S. Fähler, Appl. Phys. Lett. **97**, 222507 (2010).

[12] K. Załęski, J. Dubowik, I. Gościańska, B. Andrzejewski, and T. Toliński, Cent. Eur. J. Phys. **9**, 558 (2011).

[13] R. Vishnoi and D. Kaur, Surface Coat. Tech. **204**, 3773 (2010).

[14] T. Krenke, M. Acet, E. F. Wassermann, X. Moya, L. Mañosa, and A. Planes, Phys. Rev. B **72**, 014412 (2005).

[15] Y. Sutou, Y. Imano, N. Koeda, T. Omori, R. Kainuma, K. Ishida, and K. Oikawa, Appl. Phys. Lett. **85**, 4358 (2004).

[16] K. Otsuka, T. Ohba, M. Tokonami, and C. M. Wayman, Scr. Metall. Mater. **29**, 1359 (1993).

[17] A. Planes, L. Maosa, and M. Acet, J. Phys.: Condens. Matter **21**, 233201 (2009).

[18] L. Righi, F. Albertini, A. Paoluzi, S. Fabbrici, E. Villa, G. Calestani, and S. Besseghini, Mater. Sci. Forum **635**, 33 (2010).

[19] P. J. Brown, A. P. Gandy, K. Ishida, R. Kainuma, T. Kanomata, K.-U. Neumann, K. Oikawa, B. Ouladdiaf, and K. R. A. Ziebeck, J. Phys.: Condens. Matter **18**, 2249 (2006).

[20] M. Thomas, O. Heczko, J. Buschbeck, U. K. Rössler, J. McCord, N. Scheerbaum, L. Schultz, and S. Fähler, New J. Phys. **10**, 023040 (2008).

[21] Y. Yamada, Y. Noda, and M. Takimoto, Solid State Commun. **55**, 1003 (1985).

[22] S. Agduk and G. Gökoğlu, J. Alloys Compd. **511**, 9 (2011).

[23] M. Huang, J. Appl. Phys. **97**, 064906 (2005).

[24] B. Zhang, X. X. Zhang, S. Y. Yu, J. L. Chen, Z. X. Cao, and G. H. Wu, Appl. Phys. Lett. **91**, 012510 (2007).

[25] V. N. Antonov, A. Y. Perlov, P. M. Oppeneer, A. N. Yaresko, and S. V. Halilov, Phys. Rev. Lett. **77**, 5253 (1996).

[26] P. Pörsch, M. Kallmayer, T. Eichhorn, G. Jakob, H. J. Elmers, C. A. Jenkins, C. Felser, R. Ramesh, and M. Huth, Appl. Phys. Lett. **93**, 022501 (2008).

[27] A. Hamzic, R. Asomoza, and I. A. Campbee, J. Phys. F **11**, 1441 (1981).

[28] K. Koyama, H. Okada, K. Watanabe, T. Kanomata, R. Kainuma, W. Ito, K. Oikawa, and K. Ishida, Appl. Phys. Lett. **89**, 182510 (2006).

[29] Y. C. Shu, Arch. Rational Mech. Anal. **153**, 39 (2000).

[30] T. Krenke, M. Acet, E. F. Wassermann, X. Moya, L. Mañosa, and A. Planes, Phys. Rev. B **73**, 174413 (2006).

[31] Q. Meng, Y. Rong, and T. Y. Hsu, Phys. Rev. B **65**, 174118 (2002).

[32] R. F. Hamilton, H. Sehitoglu, Y. Chumlyakov, and H. J. Maier, Acta Mater. **52**, 3383 (2004).